Proceedings of the XIII International Conference "Ion Implantation and Other Applications of Ions and Electrons"

Effect of Manganese Ion Implantation on Cavitation Erosion Resistance of HIPed Stellite 6

M. Szala[a,*], D. Chocyk[b] and M. Turek[c]

[a] *Department of Materials Engineering, Faculty of Mechanical Engineering, Lublin University of Technology, Nadbystrzycka 36D, 20-618 Lublin, Poland*
[b] *Department of Applied Physics, Faculty of Mechanical Engineering, Lublin University of Technology, Nadbystrzycka 36D, 20-618 Lublin, Poland*
[c] *Institute of Physics, Maria Curie Sklodowska University in Lublin, Pl. M. Curie-Sklodowskiej 1, 20-031 Lublin, Poland*

Doi: 10.12693/APhysPolA.142.741 *e-mail: m.szala@pollub.pl

The paper studies the influence of manganese ion implantation on the cavitation erosion behaviour of the HIPed Stellite 6. The implantation process was conducted using implantation energy 175 keV, and the fluences of implanted ions were set at 5×10^{16} Mn^+/cm^2 and 1×10^{17} Mn^+/cm^2. The microstructure of the samples was investigated using scanning electron microscopy and X-ray diffraction. The cavitation erosion tests were carried out according to the ASTM G32 standard with the stationary specimens configuration. The cavitation erosion-damaged surfaces of unimplanted and implanted samples were qualitatively investigated using scanning electron microscopy. Moreover, the phase development due to the ion implantation and cavitation erosion was analysed using the X-ray diffraction technique. The HIPed Stellite 6 microstructure is based on the cobalt-containing matrix consisting of γ (face-centred cubic) and ε (hexagonal close-packed) crystal structures and Cr_7C_3 chromium carbides. Generally, the applied implantation parameters have a minimal effect on the microstructure and erosion resistance. The X-ray diffraction analysis shows a negligible effect of implantation on the microstructure. The implantation using 1×10^{17} Mn^+/cm^2 seems the most promising for prolonging the cavitation erosion incubation stage as well as for minimalizing the material loss (30.4 mg) and erosion rate (1.8 mg/h); the unimplanted Stellite 6 shows these indicators at the comparable level of 34.5 mg and 2.0 mg/h, respectively. The study confirmed that cavitation loads induce the face-centred cubic to hexagonal close-packed phase transformation in the cobalt-based matrix. The cavitation erosion mechanism relies on the material loss initiated at the carbides/matrix interfaces. Deterioration starts with the cobalt matrix plastic deformation, weakening the restraint of Cr_7C_3 carbides in the metallic matrix. First, the deformed cobalt matrix and then hard carbides are removed at the interfaces. Further, the cobalt-based matrix undergoes cracking, accelerating material removal, pits formation, and craters growth.

topics: cavitation erosion, ion implantation, manganese, cobalt alloy

1. Introduction

Ion implantation is one of the surface modification technologies that allows the deposition of different types of ions into a broad range of materials. Therefore, the literature reports on the implantation of ions such as nitrogen and manganese to improve the tribological performance [1] and of caesium to modify the properties of polyethylene terephthalate (PET) polymer [2], on the yttrium and rhenium ion implantation impact on the performance of nitride ceramic cutting tools [3], the mixed argon and nitrogen effect on the tribological performance of tool steels [4], the nitrogen ion implantation of cermet tungsten carbide (WC–Co) guide pads [5], and on many others. A few papers refer to manganese ion implantation. Budzyński et al. [6] studied the manganese ion implantation effect on the tribological behaviour of Stellite 6 and reported that, despite the reduction of the friction coefficient, the manganese ion implantation did not reduce the overall wear. On the other hand, it has been reported that the Mn-ion implantation of ultrananocrystalline diamond films has significant potential for bioimaging and vacuum electronic devices [7]. Other investigations of Mn-implanted GaN samples pointed out the implantation fluence-dependent modifications in the material properties [8]. The implantation can be utilized to improve or modify the operational properties of the solid material's surface. Significantly, the wear resistance, corrosion, or anti-erosive applications of ion

TABLE I

Chemical composition of Stellite 6 [13].

Chemical composition [wt%]									Hardness
Co	Cr	W	C	Fe	Ni	Si	Mn	Mo	
bal.	28.40	6.15	1.34	2.0	2.18	0.60	0.45	1.45	507 ± 22 HV0.2

implantation are considered in the up-to-date literature [9–11]. Different microstructural effects were reported due to the modification of metallic materials. Therefore, Sharkeev and Kozlov [12] studied the long-range effects of ion implantation, and Szala et al. [13] show that nitrogen ion implantation induces, among others, a phase transformation of cobalt alloys. These phenomena could act positively for the anti-deterioration of metallic materials.

Cavitation erosion (CE) is a common phenomenon during material degradation by micro-jets or shock waves caused by the formation and collapse of the bubbles, attributed to local pressure fluctuation [14–16]. Many different methods are used for minimalizing the deterioration action of cavitation on metallic surfaces, among others, hardfacing using the welding methods [17, 18], laser surfacing [19, 20], deposition of coating via thermal spraying of cermets [21], composites [22], ceramics [23], metallic coatings [24], deposition of physical vapour deposition (PVD) coatings [25], or plasma nitriding, and salt bath nitro-carburization [26]. One of the advanced and promising techniques for minimalizing cavitation damage is ion implantation. In fact, the literature reveals that the type of implanted element, as well as implantation process parameters, have a crucial effect on the erosion performance of metallic materials, but different equipment and ion fluence, as well as ion types, are considered. Nitrogen implantation improves the resistance to cavitation erosion of metallic materials significantly [10, 13, 27]. Unfortunately, the effect of Mn implantation in cobalt-based alloys has not been investigated.

This paper presents the preliminary studies on the effect of manganese ions implantation on the cavitation erosion resistance of the HIPed Stellite 6 (CoCrWC) alloy. Two ion fluences were compared. Special efforts were made to investigate the effect of the implantation and cavitation on the alloy phase transformations.

2. Materials and methods

The polished surfaces (Ø25 mm) of 10 mm height cylinder samples of Stellite 6 were ion-implanted, and their microstructure, phase composition, and cavitation erosion resistance were investigated in relation to the unimplanted alloy. The chemical composition of the cobalt alloy measured using X-ray fluorescence (XRF) is given in Table I [13]. Implantation was performed using the ion implantation

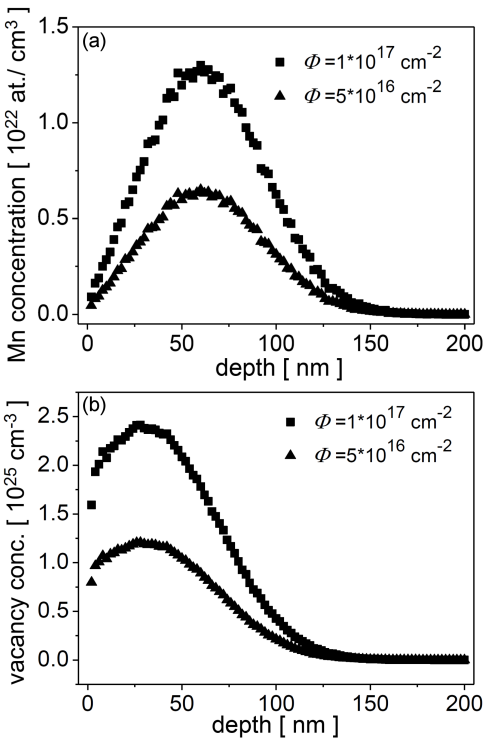

Fig. 1. Theoretical distributions of manganese ions implanted into Stellite 6 with different fluences (a); generated vacancies (b).

UNIMAS system in the Institute of Physics of Maria Curie-Skłodowska University in Lublin (Poland) and discussed in [28]. Irradiations of the alloy were done with 175 keV Mn^+ ions with fluences 5×10^{16} Mn^+/cm^2 and 1×10^{17} Mn^+/cm^2. The calculations of implanted manganese ions and radiation damage (vacancies) caused by the implantation over the sample depth were performed using the target (HIPed Stellite 6) chemical composition (Table I) and employing the commonly known SRIM (Stopping and Range of Ions in Matter) software package, available as freeware in [29]. Figure 1 shows that the maximal concentration of Mn^+ ions is found at ≈ 64 nm depth, and of radiation defects, at $\approx$ 28 nm. The effect of the ion interactions with the metallic target is much shallower than those reported for the nitrogen ions impinged on Stellite 6, studied in the previous paper [13].

Cavitation erosion was generated by a magnetostrictive-driven apparatus, resonating at 20 kHz with the peak-to-peak displacement amplitude of 50 μm as described previously [30]. The apparatus

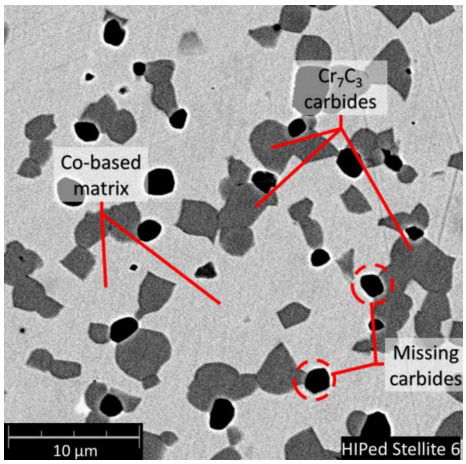

Fig. 2. Surface microstructure of the HIPed Stellite 6 (SEM).

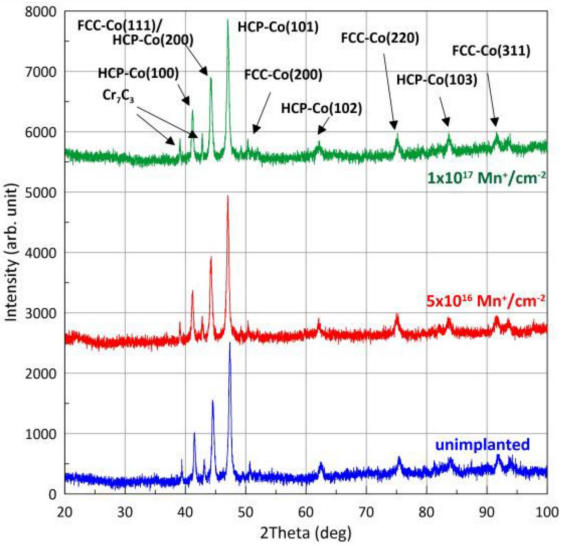

Fig. 3. Phase analysis of unimplanted and implanted HIPed Stellite 6 (XRD).

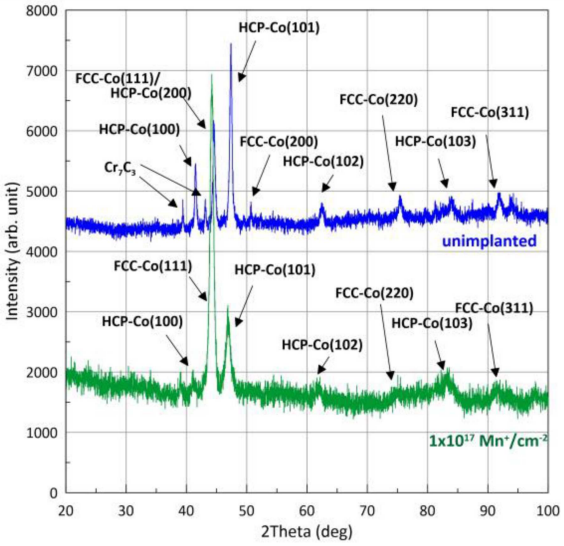

Fig. 4. Effect of cavitation erosion on the phase composition transformations of HIPed Stellite 6 (XRD).

conformed to the ASTM G32 standard [31], and the stationary specimen configuration was utilized in the experiments. The stand-off distance between the sonotrode tip and the specimen surface was set to be equal to 0.5 ± 0.05 mm. Distilled water was the testing liquid. During the specific time intervals, the mass loss was estimated with an accuracy of 0.01 mg. Therefore, the cumulative mass loss and erosion time-rate curves were plotted for the total test time lasting 24 h. The phase composition was analysed using the XRD method. The X-ray diffraction (XRD) analysis was performed in the Bragg–Brentano geometry $\theta/2\theta$, using the high-resolution diffractometer (Empyrean, Panalytical). Measurements were performed using the Cu K_α ($\lambda = 1.5418$ Å) radiation with a tube operated with a generator voltage of 45 kV and a current of 35 mA. The K-Beta Ni filter was applied. X-ray diffraction data were collected over the range of $2\theta = 20$–$100°$ with the step size $2\theta = 0.01°$ and counting time 6 s per data point, using the proportional detector. The radiation was detected with a proportional detector. The source divergence and detector slit were 1/4, and Soller's slits were used. The crystalline phase of the samples was identified using the HighScore Plus software package. The XRD analysis was conducted for the unimplanted and implanted surfaces, and the results were compared with XRD done for the cavitation-eroded samples. Finally, the eroded surfaces were analysed using scanning electron microscopy (SEM) to reveal the CE failure mechanism.

3. Results and discussion

The SEM and XRD investigations confirmed that the microstructure of HIPed Stellite 6 consists of a cobalt-based metallic matrix and second phases — mainly the hard chromium carbides type Cr_7C_3 (see Fig. 2) which is consistent with the literature data [32, 33]. The cobalt-based matrix includes γ (FCC — face-centred cubic) and ε (HCP — hexagonal close-packed) crystal structures (see Fig. 3). The implantation did not change the ratio of FCC to HCP phases followed by the comparative XRD analysis. On the other hand, cavitation erosion (CE) initiates the development of the Stellite 6 microstructure (see Fig. 4). Therefore, the difference in the FCC to HCP ratios between the uneroded and cavitation eroded samples is pronounced. The initial sample shows the domination of grains of FCC-Co (111) mixed with the HCP (101) grains arranged in the direction perpendicular to the sample surface. CE results in the partial FCC grains phase transformation to the HPC structure, which

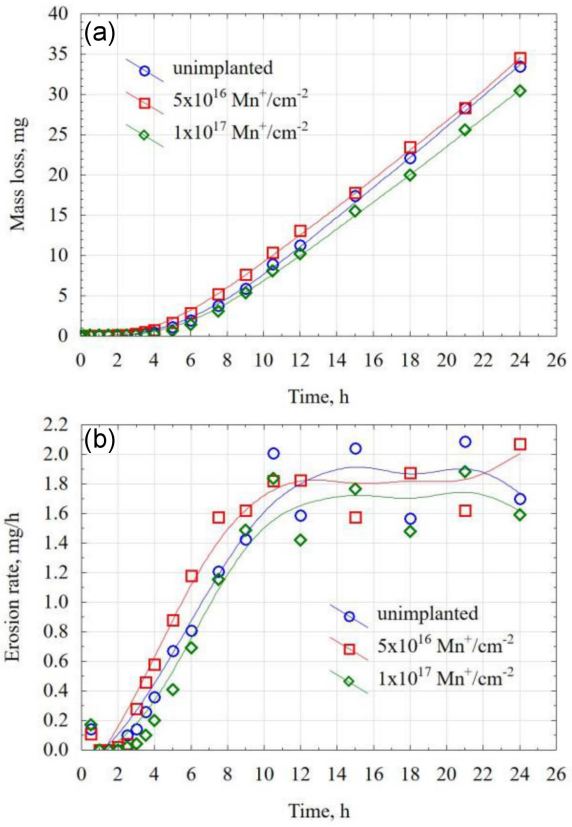

Fig. 5. Cavitation erosion mass loss (a) and rate-time (b) curves of ion-implanted and unimplanted HIPed Stellite 6.

TABLE II

Cavitation erosion results of unimplanted and ion-implanted Stellite 6

Sample	Parameter		
	Cumulative mass loss [mg]	Cumulative erosion depth [μm]	Max. erosion rate [mg/h]
unimplanted	33.51	20.68	2.09
5×10^{16} Mn^+/cm^2	34.56	21.32	2.07
1×10^{17} Mn^+/cm^2	30.42	18.77	1.88

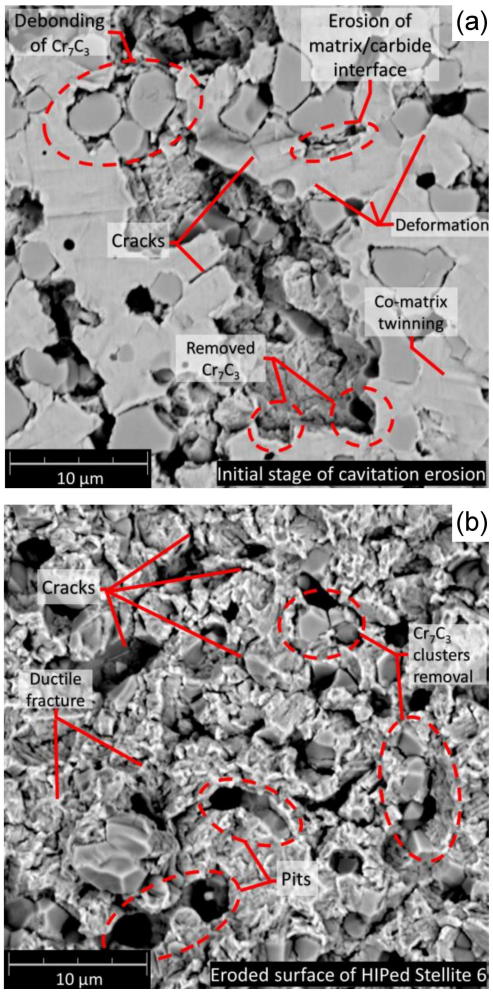

Fig. 6. Cavitation eroded surfaces in the initial stage (a) and the final stage (b) of CE testing (SEM).

was reported in the literature [13, 34]. No dominant crystallographic direction and stochastic grain arrangement are visible in this case. The SRIM calculations (Fig. 1) confirm that the effect of the manganese ion interactions with the metallic target is a few times shallower than those reported for the nitrogen ions, even if nitrogen was implanted with a smaller energy (120 keV), which was studied in the previous paper [13]. Even though the XRD analysis suggests that these implantation parameters did not imply essential changes in the phase composition of the surface layer, Stellite 6 implanted with 1×10^{17} Mn^+/cm^{-2} shows the longest incubation stage of erosion and the smallest material loss (Table II and Fig. 5). Contrary to that, the 5×10^{16} Mn^+/cm^2 implanted sample has a material loss comparable to that of the unimplanted sample. This suggests that optimizing the implantation parameters is necessary for obtaining a significant increase in the CE resistance of the cobalt alloy.

The analysis of cavitation curves confirms the presence of a peak in the initial stage of erosion rate curves (Fig. 5a), which in turn confirms the removal of poorly bound Cr_7C_3carbides from the metallic matrix. Next, the removal rate slows down. The erosion rate accelerates after 2 h of exposure. The large initial loss of carbides refers to the "cleaning effect" reported in the previous studies concerning the cermet coatings, sprayed ceramics, and metal matrix composites [21, 35, 36]. Moreover, the surface discontinuities, such as matrix/carbide interfaces, facilitate the erosive action, as shown in Fig. 6a. The detailed SEM observations show a comparable overview of the eroded surfaces in the initial and final stages of CE testing observed in the ion-implanted and unimplanted samples. Overall, the initial stage of the erosion mechanism of

HIPed Stellite 6 is comparable to those reported for the metal matrix composites (steel and cast iron reinforced by TiC [36]), where the reinforcing ceramic particles undergo erosion first. The synthesis of information given in Figs. 5 and 6 confirms that the CE mechanism of HIPed Stellite 6 is related to the material loss initiated at the carbides/matrix interfaces. Deterioration starts with the cobalt matrix plastic deformation, weakening the restraint of carbides in the metallic matrix. Then the hard carbides are removed. Moreover, the cavitation loads contribute to the strain-induced FCC to HCP phase martensitic transformation, revealed by XRD (Fig. 4). The systematically deformed cobalt matrix undergoes cracking, accelerating material removal as well as initiating the pits formation and craters growth.

4. Conclusions

The paper presents the effect of manganese ions implantation on the cavitation erosion (CE) resistance of HIPed Stellite 6 alloy. The following conclusions are drawn:

- The manganese ion implantation utilizing the energy 175 keV and the fluences of implanted ions at 5×10^{16} Mn^+/cm^2 and 1×10^{17} Mn^+/cm^2 have a minimal effect on the microstructure and erosion resistance. Therefore, the initial structure of HIPed Stellite 6 consists of a cobalt-based matrix consisting of γ (FCC — face-centred cubic) and ε (HCP — hexagonal close-packed) crystal structures and Cr_7C_3 chromium carbides. Manganese ion implantation did not result in phase transformation as it was in the case of nitrogen ion implantation [13].
- Compared to the unimplanted HIPed Stellite 6, the ion implantation using 1×10^{17} Mn^+/cm^2 seems the most promising for prolonging the cavitation erosion incubation stage and minimalizing the material loss (30.4 mg) and erosion rate (1.8 mg/h), while unimplanted Stellite 6 shows these indicators at a comparable level of 34.5 mg and 2.0 mg/h, respectively.
- The XRD analysis of eroded surfaces indicates that CE induces the FCC to HCP martensitic phase transformation of the cobalt-based matrix.
- Cavitation erosion mechanisms consist of the material loss initiated at the carbides/matrix interfaces. Deterioration starts with the cobalt matrix plastic deformation, weakening the restraint of carbides in the metallic matrix. Then, the cobalt-based matrix and further hard carbides are removed at the interfaces. Finally, a deformed cobalt matrix undergoes cracking, accelerating material removal and formation of pits and craters growth.

References

[1] M. Kamiński, P. Budzyński, M. Szala, M. Turek, *IOP Conf. Ser. Mater. Sci. Eng.* **421**, 032012 (2018).

[2] M. Musiatowicz, M. Turek, A. Droździel, K. Pyszniak, W. Grudziński, *Adv. Sci. Technol. Res. J.* **16**, (2022).

[3] D. Morozow, Z. Siemiątkowski, E. Gevorkyan, M. Rucki, J. Matijošius, A. Kilikevičius, J. Caban, Z. Krzysiak, *Materials* **13**, 4687 (2020).

[4] P. Budzynski, J. Filiks, P. Żukowski, K. Kiszczak, M. Walczak, *Vacuum* **78**, 685 (2005).

[5] D. Morozow, M. Barlak, Z. Werner et al., *Materials* **14**, 239 (2021).

[6] P. Budzyński, M. Kamiński, M. Turek, M. Wiertel, *Wear* **456–457**, 203360 (2020).

[7] S. Kunuku, C.-H. Chen, P.-Y. Hsieh, B.-R. Lin, N.-H. Tai, H. Niu, *Appl. Phys. Lett.* **114**, 131601 (2019).

[8] A. Majid, N. Ahmad, M. Rizwan, S.U.-D. Khan, F.A.A. Ali, J. Zhu, *J. Electron. Mater.* **47**, 1555 (2018).

[9] P. Budzyński, M. Kamiński, Z. Surowiec, M. Wiertel, V.A. Skuratov, E.A. Korneeva, *Tribol. Int.* **156**, 106854 (2021).

[10] S. Verma, P. Dubey, A.W. Selokar, D.K. Dwivedi, R. Chandra, *Trans. Indian Inst. Met.* **70**, 957 (2017).

[11] F. Wang, C. Zhou, L. Zheng, H. Zhang, *Appl. Surf. Sci.* **392**, 305 (2017).

[12] Yu.P. Sharkeev, E.V. Kozlov, *Surf. Coat. Technol.* **158–159**, 219 (2002).

[13] M. Szala, D. Chocyk, A. Skic, M. Kamiński, W. Macek, M. Turek, *Materials* **14**, 2324 (2021).

[14] Z. Qin, X. Li, D. Xia, Y. Zhang, C. Feng, Z. Wu, W. Hu, *Ultrason. Sonoch.* **89**, 106143 (2022).

[15] L. Wang, N. Qiu, D.-H. Hellmann, X. Zhu, *J. Mech. Sci. Technol.* **30**, 533 (2016).

[16] C.H. Tang, F.T. Cheng, H.C. Man, *Mater. Sci. Eng. A* **373**, 195 (2004).

[17] M. Szala, M. Walczak, T. Hejwowski, *Adv. Sci. Technol. Res. J.* **15**, 376 (2021).

[18] A.V. Fedorov, A.I. Rymkevich, V.V. Bazhenov, A.S. Zubchenko, N.V. Davydova, *Weld. Int.* **29**, 894 (2015).

[19] Q. Zhang, L. Wu, H. Zou, B. Li, G. Zhang, J. Sun, J. Wang, J. Yao, *J. Alloys Compd.* **860**, 158417 (2021).

[20] I. Mitelea, I. Bordeasu, I.D. Utu, O. Karancsi, *Mater. Plast.* **53**, 29 (2016).

[21] E. Jonda, M. Szala, M. Sroka, L. Łatka, M. Walczak, *Appl. Surf. Sci.* **608**, 155071 (2023).

[22] Z. Wei, Y. Wu, S. Hong, J. Cheng, L. Qiao, J. Cheng, S. Zhu, *Ceram. Int.* **47**, 15121 (2021).

[23] L. Łatka, M. Michalak, M. Szala, M. Walczak, P. Sokołowski, A. Ambroziak, *Surf. Coat. Technol.* **410**, 126979 (2021).

[24] M. Szala, M. Walczak, L. Łatka, K. Gancarczyk, D. Özkan, *Adv. Mater. Sci.* **20**, 26 (2020).

[25] A.K. Krella, *Wear* **478–479**, 203762 (2021).

[26] C.V. Roa, J.A. Valdes, F. Larrahondo, S.A. Rodríguez, J.J. Coronado, *J. Mater. Eng. Perform.* **30**, 7195 (2021).

[27] A. Karimi, *Acta Metall.* **37**, 1079 (1989).

[28] M. Turek, A. Drozdziel, K. Pyszniak, S. Prucnal, D. Maczka, Yu.V. Yushkevich, Yu.A. Vaganov, *Instrum. Exp. Tech.* **55**, 469 (2012).

[29] J.F. Ziegler, SRIM software package.

[30] M. Szala, A. Dudek, A. Maruszczyk, M. Walczak, J. Chmiel, M. Kowal, *Acta Phys. Pol. A* **136**, 335 (2019).

[31] ASTM G32-10, "Standard Test Method for Cavitation Erosion Using Vibratory Apparatus", ASTM International, West Conshohocken (PA) 2010.

[32] V.L. Ratia, D. Zhang, M.J. Carrington, J.L. Daure, D.G. McCartney, P.H. Shipway, D.A. Stewart, *Wear* **426–427**, 1222 (2019).

[33] U. Malayoglu, A. Neville, *Wear* **255**, 181 (2003).

[34] Š. Houdková, Z. Pala, E. Smazalová, M. Vostřák, Z. Česánek, *Surf. Coat. Technol.* **318**, 129 (2017).

[35] M. Nowakowska, L. Łatka, P. Sokołowski, M. Szala, F.-L. Toma, M. Walczak, *Wear* **508–509**, 204462 (2022).

[36] Ł. Szymański, E. Olejnik, J.J. Sobczak, M. Szala, P. Kurtyka, T. Tokarski, A. Janas, *J. Mater. Process. Technol.* **308**, 117688 (2022).